Electronic structure and x-ray magnetic circular dichroism in ferroelectric $CaMnTi_2O_6$

V. N. Antonov,[1,2] D. A. Kukusta,[1,3] S. V. Moklyak,[1] D. V. Mazur,[1] and L. V. Bekenov[1]
[1]*G. V. Kurdyumov Institute for Metal Physics of the N.A.S. of Ukraine, 36 Academician Vernadsky Boulevard, UA-03142 Kyiv, Ukraine*
[2]*University of Bialystok, K. Ciolkowskiego 1M, PL-15-245 Bialystok, Poland*
[3]*Max-Planck-Institut für Festkörperforschung, Heisenberg Strasse 1, D-70569 Stuttgart, Germany*

(Received 10 October 2019; revised manuscript received 24 January 2020; accepted 18 February 2020; published 27 February 2020)

We study the electronic and magnetic properties of ferroelectric $CaMnTi_2O_6$ within density functional theory using the generalized gradient approximation (GGA) with the consideration of strong Coulomb correlations (GGA + U) in the framework of the fully relativistic spin-polarized Dirac linear muffin-tin orbital band structure method. The x-ray absorption spectra (XAS) and x-ray magnetic circular dichroism (XMCD) at the Mn, Ti $L_{2,3}$, and O K edges have been investigated theoretically. The calculated results are in good agreement with experimental data. The core-hole effect in the final state as well as the effect of the electric quadrupole E_2 and magnetic dipole M_1 transitions have been investigated. The core-hole effect has improved the agreement with the experimental XAS and XMCD spectra at the Ti and Mn $L_{2,3}$ edges.

DOI: 10.1103/PhysRevB.101.054441

I. INTRODUCTION

Multiferroics (MFs) are compounds where long-range magnetic and electric dipolar orders coexist [1]. There is plenty of fascinating physics in these materials, owing to the strong entanglement of spin-charge-orbital degrees of freedom [2,3], and they have great potential for technological applications in energy-efficient information processing and storage [4–6]. For widespread implementation of new technology, the coexistence of long-range magnetic and electric orders at room temperature will be required; at present, there is only one material, $BiFeO_3$, known to exhibit ferroelectric and antiferromagnetic (AFM) orders above room temperature [7]. Recently, several manganese and iron oxides have been shown to be strong-coupling materials promising for realizing room-temperature multiferroics. However, ferroelectricity in these materials is rather weak [8].

So far, room-temperature ferroelectric materials are generally associated with single perovskites based on second-order Jahn-Teller (SOJT) active cations with d^0 (Ti^{4+}, Zr^{4+}, Nb^{5+}) or s^2 (Pb^{2+}, Bi^{3+}) valence band electron configurations. These SOJT active cations are prone to anisotropic covalent bonding with ligands inducing structural distortions that may eventually lead to the appearance of a collective polar mode and a macroscopic electric dipolar moment **P**, whenever the relevant distortions do not array generating antiparallel effects [9]. Recently, Aimi *et al.* [10] synthesized a new tetragonal double perovskite ferroelectric $CaMnTi_2O_6$ with less common A-site order and proved that A-site ordering and SOJT distortions can couple to enable ferroelectricity. Gou *et al.* [11] identified the origin of the ferroelectricity in $CaMnTi_2O_6$ using first-principles calculations combined with detailed symmetry analyses. They explored the properties of $CaMnTi_2O_6$ including its ferroelectric polarization, dielectric and piezoelectric responses, magnetic order, electronic structure, and optical absorption coefficient. It was found that $CaMnTi_2O_6$ exhibits room-temperature-stable ferroelectricity and moderate piezoelectric responses. Soft x-ray absorption and magnetic circular dichroism in $CaMnTi_2O_6$ were measured recently by Herrero-Martin *et al.* [9]. $CaMnTi_2O_6$ presents a new class of ferroelectric perovskites for potential applications in ferroelectric photovoltaic solar cells.

The aim of this paper is the theoretical study from first principles of the electronic and magnetic structures and x-ray magnetic circular dichroism in the ferroelectric $CaMnTi_2O_6$ compound. The energy band structure of ferroelectric $CaMnTi_2O_6$ is calculated within the *ab initio* approach taking into account strong electron correlations by applying a local spin-density approximation (LSDA) to density functional theory supplemented by a Hubbard U term [generalized gradient approximation (GGA) + U] [12].

The paper is organized as follows. The computational details are presented in Sec. II. Section III presents the electronic structure, x-ray absorption spectra (XAS), and x-ray magnetic circular dichroism (XMCD) of ferroelectric $CaMnTi_2O_6$ at the Mn, Ti $L_{2,3}$, and O K edges calculated in the GGA + U approximation. Theoretical results are compared to the experimental measurements. Finally, the results are summarized in Sec. IV.

II. CRYSTAL STRUCTURE AND COMPUTATIONAL DETAILS

A. X-ray magnetic circular dichroism

Magneto-optical (MO) effects refer to various changes in the polarization state of light upon interaction with materials possessing a net magnetic moment, including rotation of the plane of linearly polarized light (Faraday, Kerr rotation) and the complementary differential absorption of left and right circularly polarized light (circular dichroism). In the near-visible spectral range these effects result from excitation of electrons in the conduction band. Near x-ray absorption edges,

or resonances, magneto-optical effects can be enhanced by transitions from well-defined atomic core levels to empty valence or conduction states.

Within the one-particle approximation, the absorption coefficient $\mu_j^\lambda(\omega)$ for incident x-ray polarization λ and photon energy $\hbar\omega$ can be determined as the probability of electronic transitions from initial core states with the total angular momentum j to final unoccupied Bloch states,

$$\mu_j^\lambda(\omega) = \sum_{m_j}\sum_{n\mathbf{k}} |\langle\Psi_{n\mathbf{k}}|\Pi_\lambda|\Psi_{jm_j}\rangle|^2 \delta\left(E_{n\mathbf{k}} - E_{jm_j} - \hbar\omega\right) \times \theta(E_{n\mathbf{k}} - E_F), \quad (1)$$

where Ψ_{jm_j} and E_{jm_j} are the wave function and the energy of a core state with the projection of the total angular momentum m_j, $\Psi_{n\mathbf{k}}$ and $E_{n\mathbf{k}}$ are the wave function and the energy of a valence state in the nth band with the wave vector $\mathbf{k}$, and E_F is the Fermi energy.

Π_λ is the electron-photon interaction operator in the dipole approximation

$$\Pi_\lambda = -e\boldsymbol{\alpha}\mathbf{a}_\lambda, \quad (2)$$

where $\boldsymbol{\alpha}$ are the Dirac matrices and $\mathbf{a}_\lambda$ is the λ polarization unit vector of the photon vector potential, with $a_\pm = 1/\sqrt{2}(1, \pm i, 0)$, $a_\parallel = (0, 0, 1)$. Here, $+$ and $-$ denote, respectively, left and right circular photon polarizations with respect to the magnetization direction in the solid. Then, x-ray magnetic circular and linear dichroism are given by $\mu_+ - \mu_-$ and $\mu_\parallel - (\mu_+ + \mu_-)/2$, respectively. More detailed expressions of the matrix elements in the electric dipole approximation may be found in Refs. [13–15]. The matrix elements due to magnetic dipole and electric quadrupole corrections are presented in Ref. [15].

Concurrent with the development of the x-ray magnetic circular dichroism experiment, some important magneto-optical sum rules have been derived [16–19].

For the $L_{2,3}$ edges the l_z sum rule can be written as [14]

$$\langle l_z\rangle = n_h \frac{4\int_{L_3+L_2} d\omega(\mu_+ - \mu_-)}{3\int_{L_3+L_2} d\omega(\mu_+ + \mu_-)}, \quad (3)$$

where n_h is the number of holes in the d band $n_h = 10 - n_d$, and $\langle l_z\rangle$ is the average of the magnetic quantum number of the orbital angular momentum. The integration is taken over the whole $2p$ absorption region. The s_z sum rule can be written as

$$\langle s_z\rangle + \frac{7}{2}\langle t_z\rangle = n_h \frac{\int_{L_3} d\omega(\mu_+ - \mu_-) - 2\int_{L_2} d\omega(\mu_+ - \mu_-)}{\int_{L_3+L_2} d\omega(\mu_+ + \mu_-)}, \quad (4)$$

where t_z is the z component of the magnetic dipole operator $\mathbf{t} = \mathbf{s} - 3\mathbf{r}(\mathbf{r}\cdot\mathbf{s})/|\mathbf{r}|^2$ which accounts for the asphericity of the spin moment. The integration $\int_{L_3}$ ($\int_{L_2}$) is taken only over the $2p_{3/2}$ ($2p_{1/2}$) absorption region.

B. Crystal structure

It was revealed by Aimi *et al.* [10] that $CaMnTi_2O_6$ possesses the noncentrosymmetric space group $P4_2mc$ (No. 105), which is a subgroup of $P4_2/mmc$. To the best of our knowledge, this compound is the first example of an oxide adopting the space group $P4_2mc$. The crystal structure of $CaMnTi_2O_6$ is shown in Fig. 1. This tetragonal structure has two Mn^{2+} sites, two Ca^{2+} sites, one Ti^{4+} site, and five O^{2-} sites. The crystal parameters of $CaMnTi_2O_6$ are presented in Table I.

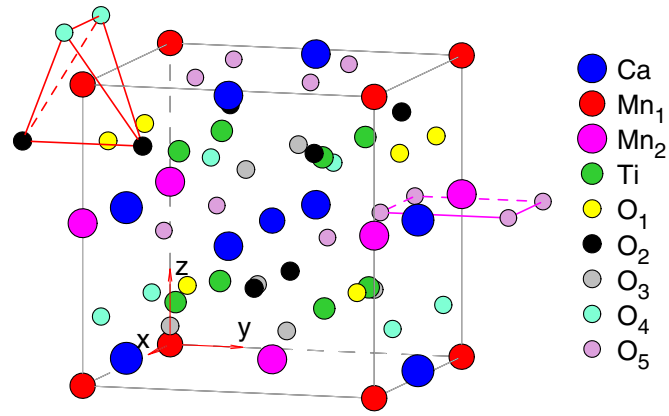

FIG. 1. Crystal structure of ferroelectric $CaMnTi_2O_6$ (the space group is $P4_2mc$, No. 105). Red and magenta spheres represent Mn atoms, blue and green spheres show Ca and Ti atoms, respectively.

The octahedral B positions are occupied by Ti^{4+} ions. In the A site, Ca^{2+} ions alternate with Mn^{2+} along the a and b axes forming a columnar ordered structure. In addition, the two Mn positions exhibit different coordination: tetrahedral at Mn_1 sites and pseudosquare planar at Mn_2 (Fig. 1). In contrast to the centrosymmetric double perovskite structure adopted by $CaFeTi_2O_6$ ($P4_2/nmc$) [20], Ti^{4+} ions in $CaMnTi_2O_6$ are shifted from the basal plane of the octahedron along the c axis, losing spatial inversion [10]. These distortions result in a polar structure. Similar to that of $CaFeTi_2O_6$, the structure of $CaMnTi_2O_6$ is based on a framework of corner-sharing TiO_6 octahedra with the $a^+a^+c^-$ tilting in Glazer's notation [21] and the Mn^{2+} and Ca^{2+} ions are ordered into columns directed along the c axis. For their part, the Mn^{2+} ions with square-planar coordination suffer a similar displacement (see the shift of Mn_2 atoms along the z direction in Fig. 1). Indeed, the reduced crystal field energy provided by their d^5 valence band configuration allows high coordination symmetry freedom. As

TABLE I. Atomic positions of $CaMnTi_2O_6$ (space group $P4_2mc$, No. 105) at room temperature (lattice constant $a = 7.5376$ Å and $c = 7.6002$ Å [9]).

Atom	Site	x	y	z
Ca_1	$2a$	0	0	0
Ca_2	$2b$	0.5	0.5	0.0385
Mn_1	$2c$	0	0.5	0.5162
Mn_2	$2c$	0	0.5	0.0557
Ti	$8f$	0.255	0.2461	0.270
O_1	$4e$	0.291	0.5	0.289
O_2	$4d$	0.294	0	0.820
O_3	$4d$	0.202	0	0.227
O_4	$4e$	0.210	0.5	0.717
O_5	$8f$	0.1976	0.2805	0.013

a consequence, a remnant polarization of 3.5 mC/cm^2 gets measured at room temperature [9].

C. Calculation details

The details of the computational method are described in our previous papers [22–25] and here we only mention several aspects. The band structure calculations were performed using the fully relativistic linear muffin-tin orbital (LMTO) method [14,26], which uses four-component basis functions constructed by solving the Dirac equation inside an atomic sphere [27]. The exchange-correlation functional of a GGA type was used in the version of Perdew, Burke, and Ernzerhof (PBE) [28]. The Brillouin zone (BZ) integration was performed using the improved tetrahedron method [29] and the self-consistent charge density was obtained with 4096 **k** points in the BZ. After achievement of the convergency the XAS and XMCD spectra were calculated on the mesh of 13 824 **k** points in the BZ. The basis consisted of Ca, Mn, and Ti s, p, d, and f and O s, p, and d LMTOs.

We found that the agreement between the theoretically calculated and experimentally measured XAS and XMCD spectra became much better with taking into account strong Coulomb correlations. To include the electron-electron correlations into the consideration we used the "relativistic" generalization of the rotationally invariant version of the LSDA + U method [30], which takes into account SO coupling so that the occupation matrix of localized electrons becomes nondiagonal in spin indexes. This method is described in detail in our previous paper [30] including the procedure to calculate the screened Coulomb U and exchange J integrals, as well as the Slater integrals F^2, F^4, and F^6.

The screened Coulomb U and exchange Hund coupling J_H integrals enter the LSDA + U energy functional as external parameters and have to be determined independently. These parameters can be determined from supercell LSDA calculations using the Slater's transition state technique [31,32], from constrained LSDA calculations (cLSDA) [32–36], or from the constrained random-phase approximation (cRPA) scheme [37]. Subsequently, a combined cLSDA and cRPA method was also proposed [38]. The cLSDA calculations produce $J_H = 0.9$ eV and 0.85 eV for the Mn and Ti sites in $CaMnTi_2O_6$, respectively. It is known that the cRPA method underestimates the values of U in some cases [39]. On the other hand, the cLSDA method produces too large values of U [40]. Therefore, in our calculations we treated the Hubbard U as an external parameter and varied it from 3.0 to 7.0 eV. We adjusted the value of U to achieve the best agreement with the experiment. We found that the values of $U_{\text{eff}} = U - J_H =$ 3.1 eV and 3.15 eV for Mn and Ti, respectively, give the best agreement between the calculated and experimental XMCD spectra in $CaMnTi_2O_6$. Our calculations can be considered as calculations from first principles with one additional parameter U_{eff}.

The x-ray absorption and dichroism spectra were calculated taking into account the exchange splitting of core levels. The finite lifetime of a core hole was accounted for by folding the spectra with a Lorentzian. The widths of core levels $\Gamma_{L_{2,3}}$ for Mn and Ti and Γ_K for O were taken from Ref. [41]. The finite experimental resolution of the spectrometer was accounted for by a Gaussian of 0.6 eV (the s coefficient of the Gaussian function).

In the x-ray absorption process an electron is promoted from a core level to an unoccupied state, leaving a core hole. As a result, the electronic structure at this state differs from that of the ground state. In order to reproduce the experimental spectrum the self-consistent calculations should be carried out including a core hole. In this study the core-hole effect was fully taken into account in the self-consistent iterations by removing an electron at the core orbital using the supercell approximation. The core state of the target atom in the ground state provides the initial state $|i\rangle$ for the spectral calculation. The final states $|f\rangle$ are the conduction band states obtained separately by the calculations in which one of the core electrons of the target atom is placed at the lowest conduction band. The interaction and the screening of the electron-hole pair are fully accounted for by the self-consistent iterations of the final-state Kohn-Sham equations. This procedure simulates the experimental situation, in which the sample can easily supply an electron to screen a localized charge produced by the core hole. Such an approach considers the symmetry breaking of the system in a natural way, and self-consistently describes the charge redistribution induced by the core hole. A similar approximation has been used by several authors [42–48] for the interpretation of the x-ray absorption. However, the effect of the electron-hole interaction in the final state on the XMCD spectra has been investigated to a much lesser extent in the literature. One should mention that the effect of the electron-hole interaction in the final state is different for different edges and systems with different localization of the electronic states. For example, Ikeno and Mizoguchi [48] show that the proper introduction of the core-hole effect improves the agreement between the calculated and experimentally measured XAS spectra at the oxygen K edge in MgO. Mo and Ching [44] obtained excellent agreements with experimental XAS spectra for Si K, Si $L_{2,3}$, and O K edges in α-SiO2. The usual interpretation using the orbital-resolved local density of states in the conduction band was unsatisfactory. The final-state interaction improves the agreement between theory and experiment for the XMCD spectra at the Gd $M_{4,5}$ and N K edges in GdN; however, it has a minor influence on the shape of the Gd $L_{2,3}$ XMCD spectra [23]. We should mention also that the size of the supercell is important, and it should be large enough to inhibit the interaction between excited atoms in neighboring supercells. In our calculations we used a $2 \times 2 \times 2$ supercell. At one of the Ti (or Mn) atoms we created a hole at the $2p_{1/2}$ or $2p_{3/2}$ levels separately for the self-consistent GGA + U calculations of the L_2 and L_3 spectra, respectively.

III. ELECTRONIC STRUCTURE OF $CaMnTi_2O_6$

Band structure and DOSs of $CaMnTi_2O_6$

Usually ferroelectric oxides, such as $BaTiO_3$ and $KNbO_3$, are wide-gap ($E_g > 3.0$ eV) insulators. On the other hand, multiferroics $BiFeO_3$ ($E_g = 2.7$ eV) and Bi_2FeCrO_6 ($E_g =$ 1.4 eV) have lower band gaps suitable for absorption of visible light [11]. The self-consistent calculations reveal a semiconducting electronic structure in the AFM-ordered $CaMnTi_2O_6$ with the energy gap of 2.52 eV in the Γ symmetry point;

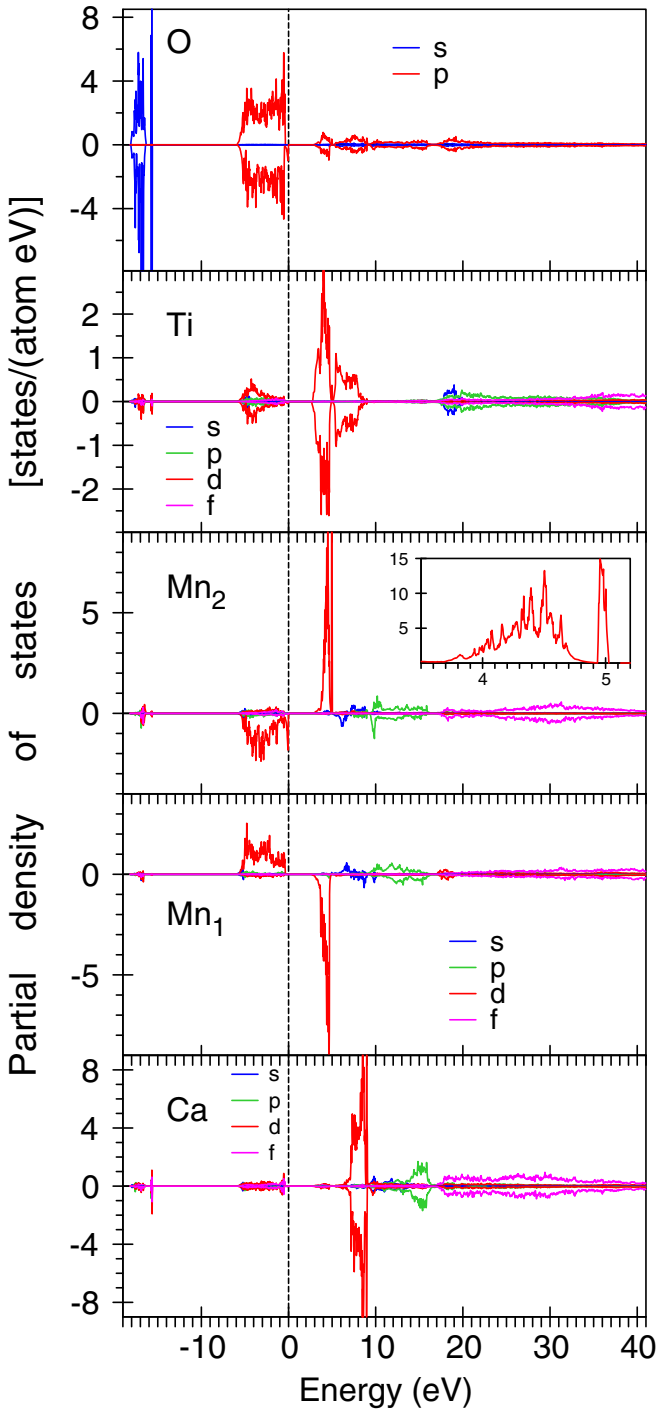

FIG. 2. Partial density of states [in states/(atom eV)] of $CaMnTi_2O_6$ in the GGA + U approximation.

therefore, $CaMnTi_2O_6$ can be used for solar energy conversion. It should be mentioned that Gou *et al.* [11] obtained a slightly larger energy gap of 2.88 eV for the C-type AFM ordering in $CaMnTi_2O_6$ using the Vienna Ab initio Simulation Package (VASP) code [49–51].

Figure 2 presents the partial density of states (PDOS) for $CaMnTi_2O_6$. The O 2s states are located mostly between −15.7 and −18.2 eV below the valence band maximum (VBM). The very narrow oxygen peak situated apart from the major 2p PDOS at −15.7 eV belongs to the O_1 site. The 2p states of the oxygen are situated from −5.9 eV to −0.3 eV; however, a small number of empty 2p oxygen states appears between 3 and 16 eV above the VBM due to their hybridization with the 3d transition metal states. The spin splitting of the oxygen 2p states is quite small (around 0.1 eV). The Ti 3d states are situated from −5.8 eV to −0.4 eV below the VBM and from 2.8 eV to 9 eV above the VBM. The Ca 3d empty states occupy the 6.8–9.2 eV energy interval, Ca 4p empty states are between 12 and 16 eV, and Ca 4f states are between 17.5 and 40 eV above the VBM.

The Mn 3d states occupy the energy interval between −5.7 eV and 0.0 eV and between 3.0 and 5.0 eV. They hybridize strongly with the oxygen 2p states. Our self-consistent calculations reveal an antiferromagnetic arrangement of the Mn magnetic moments. The two Mn positions exhibit different coordination (see Fig. 1): tetrahedral (two O_2 and two O_4 oxygen types) at the Mn_1 site and pseudosquare planar at the Mn_2 site (four O_5 oxygen types). Due to the different types of the oxygen atoms that surround the Mn ions and different Mn-O intersite distances the Mn_1 and Mn_2 ions possess different valency and different magnetic moments.

In atomic spheres (AS) approximation based calculations, partial charges are defined as integrals of electron density over the volume of the AS surrounding the atom. We found that the calculated occupation numbers from a charge integration inside a sphere surrounding the Mn ions are equal to 5.34 and 5.90 for the Mn_1 and Mn_2 sites, respectively. They are significantly larger than one would expect for a Mn ion with a d^5 configuration. From Fig. 2 one can notice, however, that apart from the Mn 3d DOSs in the energy range between −5.7 and 0 eV there is a significant O 2p contribution to the total DOS which shows an energy dependence similar to that of the Mn 3d DOS. Because of the large spatial extent of the oxygen 2p wave function the increase of the part of 3d-electron density at the Mn sites is apparently caused by the so-called "tails" of O 2p states which are a result of the decomposition of the O 2p wave function centered at O atoms inside Mn atomic spheres.

The orbital character and occupation of the localized Mn 3d states can be determined more precisely by diagonalization of the 3d occupation matrix of the GGA + U method as described in Ref. [30]. We found that the sum of the occupation numbers is equal to 4.85 and 5.25 for the Mn_1 and Mn_2 sites, respectively. This corresponds to a valency of $Mn_1^{+1.85}$ and $Mn_2^{+2.25}$. The excessive 3d charge of 0.49 and 0.65 electrons for the Mn_1 and Mn_2 sites, respectively, comes mainly from the "tails" of O 2p electrons distributed over the energy range from −5.7 to 0 eV.

The spin magnetic moments are equal to 4.525 μ_B and −4.632 μ_B for Mn_1 and Mn_2, respectively (Table II). The shapes of the 3d partial DOSs also differ from each other. There is a small energy gap of 0.25 eV between the occupied 3d PDOS and the VBM energy for the Mn_1 site. On the other hand, there is a strong peak at −0.1 eV in the 3d PDOS without an energy gap at the Mn_2 site. Besides, the Mn_2 empty 3d PDOS possesses a strong narrow peak at 5 eV above the VBM, which is absent at the Mn_1 site. Similar peaks at −0.1 and 5 eV can be found in the oxygen 2p PDOS at O_5.

TABLE II. The theoretically calculated spin M_s, orbital M_l, and total magnetic moments (in μ_B) of $CaMnTi_2O_6$.

Atom	M_s	M_l	M_{total}
Ca_1	−0.0021	0.0000	−0.0021
Ca_2	0.0022	0.0000	0.0022
Mn_1	4.5251	−0.0012	4.5239
Mn_2	−4.6322	−0.0010	−4.6332
Ti	0.0143	−0.0006	0.0137
O_1	0.010	−0.00022	0.0010
O_2	0.013	−0.00002	0.013
O_3	0.005	0.00006	0.004
O_4	0.015	0.00013	0.015
O_5	−0.017	−0.00018	−0.019

Therefore, such features in the 3*d* PDOS at the Mn_2 site can be explained by a strong hybridization between the Mn_2 3*d* states and the oxygen 2*p* states of O_5 near-neighbors.

IV. X-RAY ABSORPTION AND XMCD SPECTRA IN $CaMnTi_2O_6$

A. Ti $L_{2,3}$ XAS and XMCD spectra

Figure 4 (upper panel) shows the x-ray absorption spectra (open circles) at the Ti $L_{2,3}$ edges in $CaMnTi_2O_6$ measured at 5 K [9] with a 6 T magnetic field applied along the *c* axis in comparison with the theoretically calculated ones in the GGA + *U* approximation. The Ti^{4+} cation is in octahedral coordination with oxygen where the local octahedron gets elongated along the *c* axis in $CaMnTi_2O_6$. The experimentally measured Ti $L_{2,3}$ XAS consists of four major peaks in the range of 457–469 eV. The two peaks with the lower energy are the Ti L_3 edge while the two peaks with the higher energy are Ti L_2 edges. It is well known that when a Ti ion is octahedrally coordinated, two Ti L_3 and L_2 peaks split into two main separate peaks e_g and t_{2g} [52]. The separation between these two main peaks is associated with the crystal-field splitting modified by the exchange interaction. Because the SO splitting of the core Ti 2*p* level ($\Delta E_{\text{SO}} = 5.74$ eV) and the crystal-field splitting of the Ti 3*d* states modified by the exchange interaction ($\Delta E_{\text{CF}} = 3.3$ eV) are of the same order of magnitude the L_3 and L_2 x-ray absorption spectra are strongly overlapped. The four experimentally observed intense peaks from 457 to 469 eV can be, to a first approximation, assigned to the $2p_{3/2} \rightarrow e_g$, $2p_{3/2} \rightarrow t_{2g}$, $2p_{1/2} \rightarrow e_g$, and $2p_{1/2} \rightarrow t_{2g}$ transitions, respectively. However, the $2p_{1/2} \rightarrow e_g$ and $2p_{1/2} \rightarrow t_{2g}$ transitions (L_2 spectrum) contribute also to the two low-energy peaks. The theory reproduces the energy position of all the fine structures quite well; however, the theoretically calculated spectra are much wider than the experimentally measured ones. This is clearly seen first of all for the major peaks at 458.5 eV and 461 eV. The theory also does not reproduce the experimentally observed L_3/L_2 x-ray absorption ratio. It is well known that the L_2 and L_3 absorption channels in early 3*d* transition metals with nearly empty *d* bands are strongly coupled through the photoelectron-core-hole Coulomb and exchange interactions [53–56]. This leads to a branching ratio close to 1:1, far from the statistical ratio

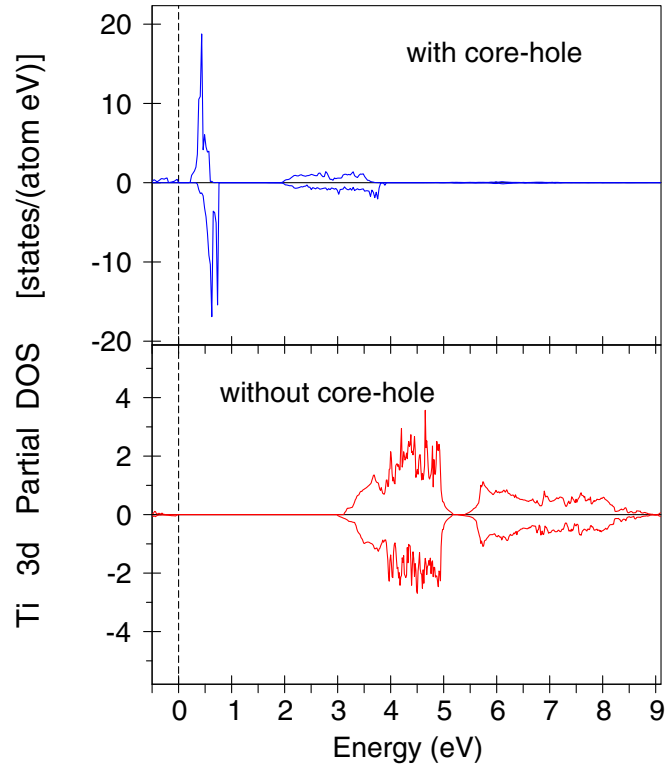

FIG. 3. Ti 3*d* partial density of states [in states/(atom eV)] of $CaMnTi_2O_6$ in the GGA + *U* approximation with taking into account the core-hole effect (upper panel) and without core-hole (lower panel) at the Ti $2p_{3/2}$ core level.

2:1, which is obtained in the single-particle theory, unless the SO interaction in the final 3*d* band is considered. From our band structure calculations we obtained the L_3/L_2 branching ratio equal to 1.65 which is far from what is experimentally observed.

We investigated the core-hole effect in the final state using the supercell approximation where the excited atom is formally treated as an impurity. We found that the core-hole interaction strongly influences Ti empty 3*d* states: they become much more narrow and shift downward by ∼4 eV (see Fig. 3).

The core-hole interaction significantly improves the agreement between theoretically calculated and experimentally measured Ti $L_{2,3}$ XAS spectra in $CaMnTi_2O_6$ (the upper panel in Fig. 4). The theory well reproduces the widths of all four major peaks in the x-ray absorption. After taking into account the core-hole effect we obtained the L_3/L_2 branching ratio equal to 1.2, which is in much better agreement with the experiment.

In spite of the nominally nonmagnetic character of Ti^{4+} (d^0), there are induced spin and orbital magnetic moments at the Ti sites due to the hybridization between the Ti *d* states and Mn *d* states in $CaMnTi_2O_6$ (see Table II). The experimental measurements recorded a tiny XMCD signal under the application of a large magnetic field [9]. The XMCD spectra at the Ti L_3 and L_2 edges show quite complicated shapes with several negative and positive peaks. The GGA + *U* approach with taking into account the core-hole effect reasonably well reproduces the shape of the two major peaks at the L_3 edge

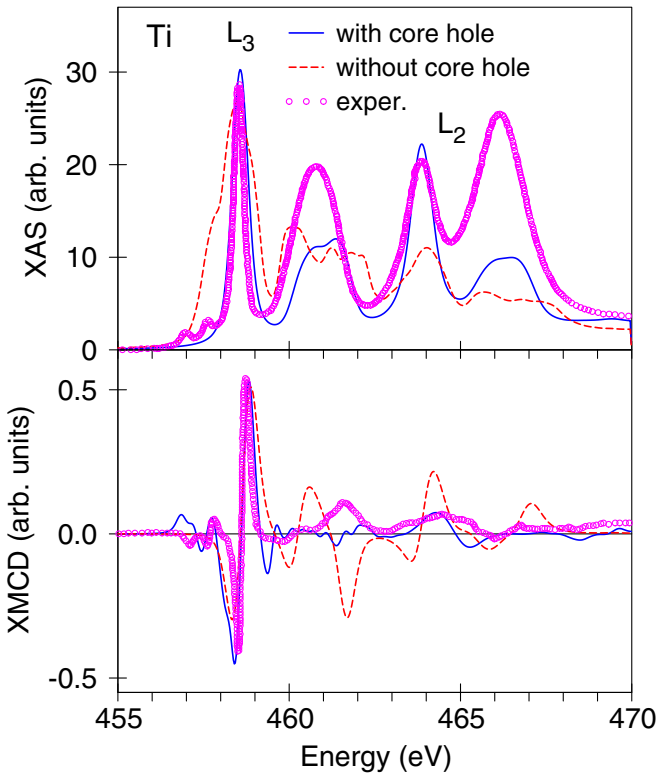

FIG. 4. Top panel: The x-ray absorption spectra (open circles) at the Ti $L_{2,3}$ edges in $CaMnTi_2O_6$ measured at 5 K [9] with a 6 T magnetic field and theoretically calculated with (full blue line) and without (dashed red curve) taking into account the core-hole effect; lower panel: the XMCD experimental (open circles) and theoretically calculated spectra of $CaMnTi_2O_6$ at the Ti $L_{2,3}$ edges taking into account the core-hole effect (full blue line) and without the core-hole effect (dashed red line).

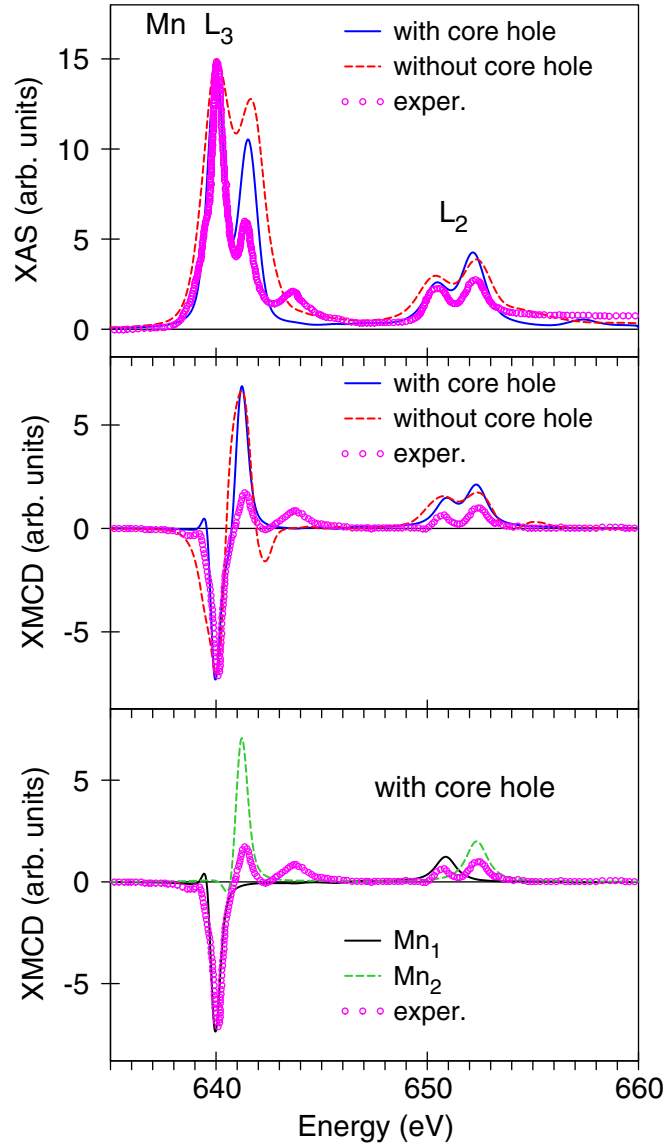

FIG. 5. Top panel: The x-ray absorption spectra (open circles) at the Mn $L_{2,3}$ edges in $CaMnTi_2O_6$ measured at 5 K [9] with a 6 T magnetic field in comparison with the theoretically calculated ones with (full blue line) and without (dashed red curve) taking into account the core-hole effect; middle panel: the XMCD experimental spectra (open circles) of $CaMnTi_2O_6$ at the Mn $L_{2,3}$ edges and the theoretically calculated ones with (full blue line) and without the core-hole effect (dashed red line) spectra; lower panel: the XMCD experimental spectra (open circles) of $CaMnTi_2O_6$ at the Mn $L_{2,3}$ edges and the theoretically calculated ones with taking into account the core-hole effect for the Mn_1 site (full black line) and for the Mn_2 site (dashed green line).

in the 457–459 eV energy interval as well as at the L_2 at 464.5 eV. Other features are reproduced with less accuracy; however, it is hard to achieve ideal agreement with the experimental measurements with such a tiny XMCD signal. The calculations without taking into account the core-hole effect visibly overestimate the dichroism in the 460–468 eV energy range.

B. Mn $L_{2,3}$ XAS and XMCD spectra

Figure 5 (upper panel) shows the x-ray absorption spectra (open circles) at the Mn $L_{2,3}$ edges in $CaMnTi_2O_6$ measured at 5 K [9] with a 6 T magnetic field applied along the c axis in comparison with the theoretically calculated ones (full blue line) in the GGA + U approximation. The Mn L_3 x-ray absorption spectrum possesses three fine structures: a major peak at 640 eV, a tiny low-energy shoulder at 637.8 eV, and two high-energy peaks at 641.4 eV and 644 eV. The theory reproduces the energy position and intensity of the major peak and shoulder at 637.8 eV quite well but fails to describe the high-energy peak at 644 eV, which probably has a satellite nature.

It is well known that XAS spectra at the transition metal $L_{2,3}$ edge are highly sensitive to the valence state: an increase of the valence state of the metal ion by 1 results in a shift of the $L_{2,3}$ XAS spectra by 1 or more eV toward higher energies, as shown by XAS studies on many oxides [57–62]. This shift is due to a final-state effect in the x-ray absorption process [63]. The energy difference between a d^n and a d^{n-1} configuration is approximately $\Delta E = E(2p^6d^{n-1} \rightarrow 2p^5d^n) - E(2p^6d^n \rightarrow 2p^6d^{n+1}) = U_{pd} - U_{dd} \sim 1$–2 eV, where U_{dd} is the Coulomb repulsion energy between two d electrons and U_{pd} is the one between a d electron and the $2p$ core hole. The Mn_1 and Mn_2 ions possess valency of 1.85+ and 2.25+,

respectively. The increase of the valence state results in a shift of the Mn_2 L_3 XAS spectrum toward higher energies in comparison with the Mn_1 L_3 XAS one. Although the L_3 XAS spectra of Mn_1 and Mn_2 have the same weights they have slightly different peak intensities due to the difference in the corresponding bandwidths.

We found that the core-hole interaction strongly influences Mn empty $3d$ states. They shift downward by ∼4 eV and become much more narrow (not shown). The latter fact significantly improves the agreement with the experiment in x-ray absorption (compare the blue and red curves in the upper panel of Fig. 5). The agreement with the experiment is also better for the Mn L_3 XMCD spectrum (the middle and lower panels of Fig. 5) with respect to the width of the negative peak at 640 eV and in the shape of the local minimum at 642 eV. The theory with taking into account the core-hole effect reproduces even the tiny low-energy peak at 639.5 eV which is absent in the calculations without this effect.

The major peaks at 640 eV and 641.4 eV in the XMCD spectra at the $L3$ edge are from AFM-arranged Mn_1 and Mn_2 atoms, respectively. The theory with or without the core-hole effect overestimates the intensity of the positive peak at 641.4 eV. These disagreements can be explained by the fact that the calculations presented in Fig. 5 have been performed for the ideal crystal structure without possible lattice imperfections and without an external magnetic field. The external magnetic field (6 T in Ref. [9]) might change the spin orientation of some Mn_2 ions, and as a result, the XMCD signal from the Mn_2 sites might be reduced. This is consistent with the strong imbalance of the spin magnetic moments of nonequivalent Mn_1 and Mn_2 sites observed experimentally [9] (see Table II).

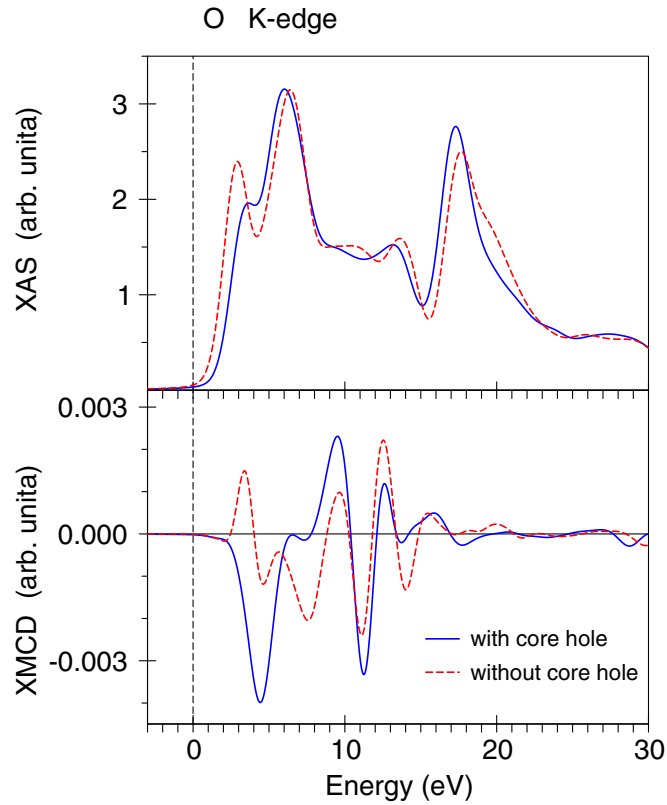

FIG. 6. Top panel: The theoretically calculated x-ray absorption spectrum at the O K edge in $CaMnTi_2O_6$ with (full blue line) and without (dashed red curve) taking into account the core-hole effect; lower panel: the theoretically calculated XMCD spectra of $CaMnTi_2O_6$ at the O K edge with (full blue line) and without (dashed red curve) taking into account the core-hole effect.

C. O K XAS and XMCD spectra

The XAS and XMCD spectra in metals and alloys at the K edge when the $1s$ core electrons are excited to empty p states through the dipole transitions are quite important. They are sensitive to the electronic states at neighboring sites because of the delocalized nature of p states.

Figure 6 presents the theoretically calculated x-ray absorption spectrum at the O K edge in $CaMnTi_2O_6$ (the red dashed curve at the top panel) and the theoretically calculated O K XMCD spectrum (the lower panel). The O K XAS spectrum extends over more then 40 eV and has the fine structures typical for the oxygen K absorption in various transition metal oxides [14].

The exchange splitting of the initial $1s$ core state is extremely small [64]; therefore only the exchange and spin-orbit splitting of the final $2p$ states is responsible for the observed dichroism at the oxygen K edge. For this reason the dichroism is found to be very small. The O K XMCD spectrum possesses a quite complicated structure with several minima and maxima. We found that the largest contribution comes from the first neighbors of the Mn_2 ions, namely, O_5 ions which possess the largest spin and orbital moments. The Mn_1 ions are surrounded by two O_2 and two O_4 ions (see Fig. 1). The induced spin magnetic moments at the O_2 and O_4 sites are aligned opposite to the O_5 spin moments (see Table II). As a result, the XMCD signal from the O_2 and O_4 sites has an opposite sign to the O_5 one reducing significantly the x-ray dichroism at the O K edge.

We investigated also the core-hole effect in the final state using the supercell approximation where the excited atom is formally treated as an impurity. Figure 7 presents the $2p$ partial density of states for different oxygen sites of $CaMnTi_2O_6$ for the valence states (left column) and conduction states (right column) with (full blue lines) and without (dashed red lines) taking into account the core-hole effect at the O K edges. The core-hole effect strongly influences the oxygen valence states: they become much more narrow and shift downward by 5 to 8 eV for different sites (see the left column of Fig. 7). The occupation numbers of the oxygen $2p$ states also increase. The conduction states (the right column of Fig. 7) are changed to a lesser extent. But still they shift downward by around 2 eV and also become more narrow.

We found that the core-hole interactions significantly alter the theoretically calculated O K XAS spectra in $CaMnTi_2O_6$ mostly in the low-energy part of the spectrum at 2–4 eV above the edge (the upper panel in Fig. 6). The core-hole effect affects the oxide K XMCD spectrum in the 2 to 10 eV energy range (the lower panel in Fig. 6), and in the 2 to 4 eV energy interval the dichroism even changes the sign.

We investigate also the effect of the electric quadrupole E_2 and magnetic dipole M_1 transitions on the XAS and XMCD spectra at the oxygen K edge. We found that the M_1 transitions

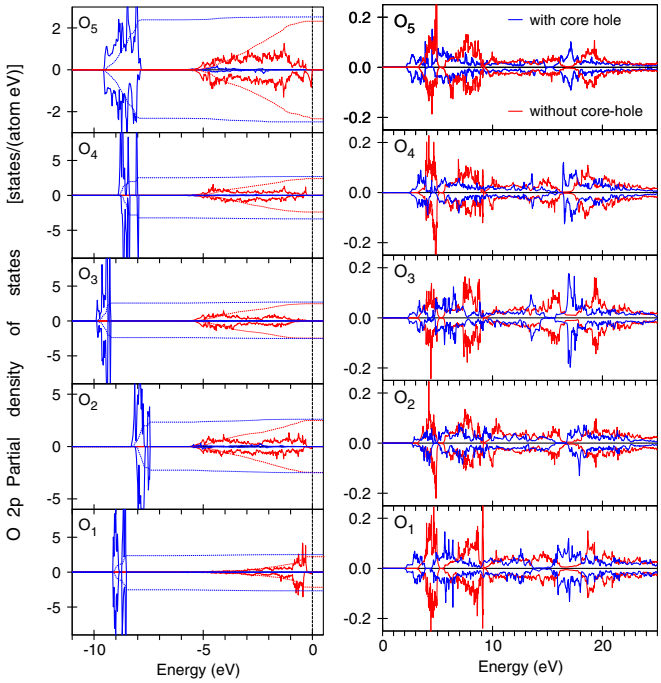

FIG. 7. The $2p$ partial density of states [in states/(atom eV)] for different oxygen sites of $CaMnTi_2O_6$ for the valence states (left column) and conduction states (right column) with (full blue lines) and without (dashed red lines) taking into account the core-hole effect at the O K edges. Dotted curves present the integrated valence partial DOSs.

are extremely small in comparison with the E_2 transitions and can be neglected. The E_2 transitions indeed contribute to the high-energy XAS and XMCD spectra, although the quadrupolar E_2 transitions are more than two orders of magnitude smaller than the electric dipole transitions E_1.

The experimental measurement of the XAS and XMCD spectra at the oxygen K edge in $CaMnTi_2O_6$ is highly desirable.

D. Magnetic moments

Our band structure calculations yield the magnetic moments for the Mn_1 ion of $M_s = 4.5251\ \mu_B$, $M_l = -0.0012\ \mu_B$, and for the Mn_2 ion of $M_s = -4.6322\ \mu_B$ and $M_l = -0.0010\ \mu_B$. The Mn spin moments are in good agreement with the results of the VASP calculations by Gou *et al.* [11] (4.57 μ_B).

The sum rules yield much smaller Mn spin moments of $M_s = 0.733\mu_B$ at 5 K and $M_s = 0.558\ \mu_B$ at 25 K (above T_N) [9]. One should mention that the XMCD technique is not able to measure the contributions from different Mn sites separately. Therefore, the sum rules provide an averaged Mn spin magnetic moment. For the AFM ordering and equivalent Mn sites one would expect zero averaged Mn spin magnetic moment. The imbalance in the Mn spin magnetic moments might be from several reasons, such as crystal imperfections (mostly due to the oxygen vacancies), the nonequivalence of the Mn_1 and Mn_2 sites due to different coordinations (tetrahedral at Mn_1 sites and pseudosquare planar at Mn_2), or the influence of the external magnetic field used in the experimental measurements (6 T) [9]. Our theoretical calculations produce a smaller magnetic imbalance of 0.1071 μ_B because we take into account only the nonequivalence of the Mn_1 and Mn_2 sites.

The experimentally estimated Mn orbital moment M_l was found to be equal to 0.026 μ_B at 5 K and 0.003 μ_B at 25 K. Both of these values are larger than the theoretical results (Table II). This discrepancy is due to the imperfection of the sum rules. The application of the sum rules to the theoretically calculated XAS and XMCD spectra produces much larger orbital magnetic moments of 0.031 μ_B as averaged by the Mn_1 and Mn_2 sites (with taking into account the core-hole effect) with better agreement with the experimental data.

Herrero-Martin *et al.* [9] estimated the values of the orbital magnetic moments in $CaMnTi_2O_6$ at the Ti site as $M_l = -0.013\ \mu_B$ using the sum rules and experimental XAS and XMCD spectra measured at 5 K and an external magnetic field of 6 T. Our band structure calculations yield the magnetic moments for the Ti atoms of $M_l = -0.0006\ \mu_B$ (see Table II). The explanation of such a disagreement is in the nature of the sum rules. The applying of the sum rules [Eq. (3)] for the theoretically calculated XAS and XMCD spectra produces the orbital magnetic moment of $M_l = -0.015\ \mu_B$ at the Ti site (with taking into account the core-hole effect) with much better agreement with the experimental estimations.

The induced spin magnetic moments at the O_1 to O_4 sites are aligned along the c axis and equal to 0.005 μ_B and 0.015 μ_B for the O_3 and O_4, respectively. The spin magnetic moments at the O_5 sites (which are the first neighbors for the Mn_2 ions) are AFM-ordered to other oxygens and have the largest spin magnetic moments of $-0.017\ \mu_B$.

The orbital magnetic moments were found to be equal to $-0.00022\mu_B$, $-0.00002\ \mu_B$, $0.00006\ \mu_B$, $0.00013\ \mu_B$, and $-0.00018\mu_B$ for the O_1, O_2, O_3, O_4, and O_5 sites, respectively. The averaged oxygen orbital magnetic moment, therefore, is equal to $-0.00023\ \mu_B$ from the self-consistent band structure calculations. The orbital sum rule applied to the theoretically calculated XAS and XMCD spectra at the oxygen K edge in the electric-dipole approximation gives the value of the orbital moment $M_l^{\mathrm{O}} = -0.00030\ \mu_B$.

V. SUMMARY

The electronic and magnetic structures as well as x-ray magnetic circular dichroism of the ferroelectric $CaMnTi_2O_6$ have been investigated theoretically within a DFT-GGA + U approach in the framework of the fully relativistic spin-polarized Dirac LMTO band structure method.

The Ca cations in $CaMnTi_2O_6$ exhibit a 10-coordinate polyhedral environment and the Mn cations display alternating tetrahedral and square-planar MnO_4 coordination. Moreover, A-site Mn^{2+} ions with high-spin states ($3d^5$) exhibit long-range AFM order in $CaMnTi_2O_6$. Due to different types of the oxygen atoms surrounding the Mn ions and different Mn-O intersite distances, Mn_1 and Mn_2 possess different valences (1.85+ and 2.25+ for the Mn_1 and Mn_2 ions, respectively) and different magnetic moments (4.527 μ_B and $-4.628\ \mu_B$ for Mn_1 and Mn_2, respectively).

We have studied the x-ray magnetic circular dichroism at the Mn and Ti $L_{2,3}$ and oxygen K edges. The calculations show good agreement with the experimental measurements. Due to the AFM ordering and different coordinations

(tetrahedral at Mn_1 sites and pseudosquare planar at Mn_2) the XMCD spectra at the Mn L_3 edge have opposite signs and are shifted to each other producing the spectrum with a major peak at 640 eV and two high-energy shoulders at 641.4 eV and 644 eV. The theory overestimates the intensity of the high-energy peak at 641.4 eV. It can be explained by the fact that the calculations have been performed for the ideal crystal structure without possible lattice imperfections and without an external magnetic field. The external magnetic field might change the spin orientation of some Mn_2 ions, and as a result, the XMCD signal from the Mn_2 sites might be reduced. The third high-energy shoulder at 644 eV in the XAS and XMCD spectra at the Mn L_3 edge probably has a satellite nature and cannot be reproduced in a one-particle approximation.

We found that the core-hole interaction strongly influences Ti and Mn empty $3d$ as well as oxygen $2p$ states: they become much more narrow and shift downward by several eV. The core-hole effect significantly improves the agreement between the theory and experiment at the Ti and Mn $L_{2,3}$ edges.

The past decade has witnessed dramatic progress in the fundamental physics of multiferroics and magnetoelectrics. The challenge and opportunity for solid-state physicists is to identify mechanisms that provide large, robust, and coupled magnetization and polarization, combined with large susceptibilities at low electric or magnetic fields, all at room temperature. Multiferroics continue to reveal novel, unanticipated physics, and the potential applications now stretch far beyond electrical control of ferromagnetism. We hope that the recent progress on the basic materials physics aspects will stimulate the physics community to dream up entirely new device paradigms that exploit the novel and unique functionalities of multiferroics.

ACKNOWLEDGMENTS

V.N.A. gratefully acknowledges the hospitality at the Faculty of Mathematics and Informatics of the University of Bialystok during his stay there. D.A.K. gratefully acknowledges the hospitality at the Max-Planck-Institut für Festkörperforschung in Stuttgart during his stay there. We are also grateful to Dr. Alexander Yaresko for helpful discussions. The studies were supported by the National Academy of Sciences of Ukraine within the budget program KPKBK 6541230-3A "Support for the development of priority areas of scientific research."

[1] K. Aizu, Phys. Rev. B **2**, 754 (1970).
[2] N. A. Spaldin and M. Fiebig, Science **309**, 391 (2005).
[3] W. Eerenstein, N. D. Mathur, and J. F. Scott, Nature (London) **442**, 759 (2008).
[4] C. Binek and B. Doudin, J. Phys.: Condens. Matter **17**, L39 (2005).
[5] M. Gajek, M. Bibes, S. Fusil, K. Bouzehouane, J. Fontcuberta, A. Barthelemy, and A. Fert, Nat. Mater. **6**, 296 (2007).
[6] C.-W. Nan, M.-I. Bichurin, S. Dong, D. Viehland, and G. Srinivasan, J. Appl. Phys. **103**, 031101 (2008).
[7] J. Wang, J. B. Neaton, H. Zheng, V. Nagarajan, S. B. Ogale, B. Liu, D. Viehland, V. Vaithyanathan, D. G. Schlom, U. V. Waghmare *et al.*, Science **299**, 1719 (2003).
[8] A. Stroppa, M. Marsman, G. Kresse, and S. Picozzi, New J. Phys. **12**, 093026 (2010).
[9] J. Herrero-Martín, J. Ruiz-Fuertes, T. Bernert, M. Koch-Müller, E. Haussühl, and J. L. García-Muñoz, Phys. Rev. B **97**, 235129 (2018).
[10] A. Aimi, D. Mori, K. Hiraki, T. Takahashi, Y. J. Shan, Y. Shirako, J. Zhou, and Y. Inaguma, Chem. Mater. **26**, 2601 (2014).
[11] G. Gou, N. Charles, J. Shi, and J. M. Rondinelli, Inorg. Chem. **56**, 11854 (2017).
[12] V. I. Anisimov, J. Zaanen, and O. K. Andersen, Phys. Rev. B **44**, 943 (1991).
[13] G. Y. Guo, H. Ebert, W. M. Temmerman, and P. J. Durham, Phys. Rev. B **50**, 3861 (1994).
[14] V. Antonov, B. Harmon, and A. Yaresko, *Electronic Structure and Magneto-Optical Properties of Solids* (Kluwer, Dordrecht, 2004).
[15] E. Arola, M. Horne, P. Strange, H. Winter, Z. Szotek, and W. M. Temmerman, Phys. Rev. B **70**, 235127 (2004).
[16] B. T. Thole and G. van der Laan, Phys. Rev. B **38**, 3158 (1988).
[17] B. T. Thole, P. Carra, F. Sette, and G. van der Laan, Phys. Rev. Lett. **68**, 1943 (1992).
[18] P. Carra, B. T. Thole, M. Altarelli, and X. Wang, Phys. Rev. Lett. **70**, 694 (1993).
[19] G. van der Laan and B. T. Thole, Phys. Rev. B **53**, 14458 (1996).
[20] J. Ruiz-Fuertes, T. Bernert, D. Zimmer, N. Schrodt, M. Koch-Muller, B. Winkler, L. Bayarjargal, C. Popescu, S. MacLeod, and K. Glazyrin, Phys. Rev. B **96**, 094101 (2017).
[21] A. M. Glazer, Acta Crystallogr. B **28**, 3384 (1972).
[22] I. Leonov, A. N. Yaresko, V. N. Antonov, U. Schwingenschlogl, V. Eyert, and V. I. Anisimov, J. Phys.: Condens. Matter **18**, 10955 (2006).
[23] V. N. Antonov, B. N. Harmon, A. N. Yaresko, and A. P. Shpak, Phys. Rev. B **75**, 184422 (2007).
[24] V. N. Antonov, A. N. Yaresko, and O. Jepsen, Phys. Rev. B **81**, 075209 (2010).
[25] B. J. Ruck, H. J. Trodahl, J. H. Richter, J. C. Cezar, F. Wilhelm, A. Rogalev, V. N. Antonov, B. D. Le, and C. Meyer, Phys. Rev. B **83**, 174404 (2011).
[26] O. K. Andersen, Phys. Rev. B **12**, 3060 (1975).
[27] V. V. Nemoshkalenko, A. E. Krasovskii, V. N. Antonov, V. N. Antonov, U. Fleck, H. Wonn, and P. Ziesche, Phys. Status Solidi B **120**, 283 (1983).
[28] J. P. Perdew, K. Burke, and M. Ernzerhof, Phys. Rev. Lett. **77**, 3865 (1996).
[29] P. E. Blöchl, O. Jepsen, and O. K. Andersen, Phys. Rev. B **49**, 16223 (1994).
[30] A. N. Yaresko, V. N. Antonov, and P. Fulde, Phys. Rev. B **67**, 155103 (2003).
[31] V. I. Anisimov and O. Gunnarsson, Phys. Rev. B **43**, 7570 (1991).
[32] I. V. Solovyev, P. H. Dederichs, and V. I. Anisimov, Phys. Rev. B **50**, 16861 (1994).
[33] P. H. Dederichs, S. Blügel, R. Zeller, and H. Akai, Phys. Rev. Lett. **53**, 2512 (1984).
[34] W. E. Pickett, S. C. Erwin, and E. C. Ethridge, Phys. Rev. B **58**, 1201 (1998).

[35] M. Cococcioni and S. de Gironcoli, Phys. Rev. B **71**, 035105 (2005).
[36] K. Nakamura, R. Arita, Y. Yoshimoto, and S. Tsuneyuki, Phys. Rev. B **74**, 235113 (2006).
[37] F. Aryasetiawan, M. Imada, A. Georges, G. Kotliar, S. Biermann, and A. I. Lichtenstein, Phys. Rev. B **70**, 195104 (2004).
[38] I. V. Solovyev and M. Imada, Phys. Rev. B **71**, 045103 (2005).
[39] V. P. Antropov, V. N. Antonov, L. V. Bekenov, A. Kutepov, and G. Kotliar, Phys. Rev. B **90**, 054404 (2014).
[40] F. Aryasetiawan, K. Karlsson, O. Jepsen, and U. Schonberger, Phys. Rev. B **74**, 125106 (2006).
[41] J. L. Campbell and T. Parr, At. Data Nucl. Data Tables **77**, 1 (2001).
[42] K. Lie, R. Hoier, and R. Brydson, Phys. Rev. B **61**, 1786 (2000).
[43] S.-D. Mo and W. Y. Ching, Phys. Rev. B **62**, 7901 (2000).
[44] S.-D. Mo and W. Y. Ching, Appl. Phys. Lett. **78**, 3809 (2001).
[45] Y.-N. Xu, Y. Chen, S.-D. Mo, and W. Y. Ching, Phys. Rev. B **65**, 235105 (2002).
[46] W.-Y. Ching, S.-D. Mo, and Y. Chen, J. Am. Ceram. Soc. **85**, 11 (2002).
[47] T. Mizoguchi, I. Tanaka, S. Yoshioka, M. Kunisu, T. Yamamoto, and W. Y. Ching, Phys. Rev. B **70**, 045103 (2004).
[48] H. Ikeno and T. Mizoguchi, Microscopy **66**, 305 (2017).
[49] P. E. Blöchl, Phys. Rev. B **50**, 17953 (1994).
[50] J. P. Perdew, K. Burke, and M. Ernzerhof, Phys. Rev. Lett. **78**, 1396 (1997).
[51] G. Kresse and D. Joubert, Phys. Rev. B **59**, 1758 (1999).
[52] A. S. Sefat, G. Amow, M. Y. Wu, G. A. Botton, and J. E. Greedan, J. Solid State Chem. **178**, 1008 (2005).
[53] J. Zaanen, G. A. Sawatzky, J. Fink, W. Speier, and J. C. Fuggle, Phys. Rev. B **32**, 4905 (1985).
[54] J. Schwitalla and H. Ebert, Phys. Rev. Lett. **80**, 4586 (1998).
[55] P. Krüger and C. R. Natoli, Phys. Rev. B **70**, 245120 (2004).
[56] A. L. Ankudinov, A. I. Nesvizhskii, and J. J. Rehr, Phys. Rev. B **67**, 115120 (2003).
[57] C. T. Chen and F. Sette, Phys. Scr. **1990**, 119 (1990).
[58] C. Mitra, Z. Hu, P. Raychaudhuri, S. Wirth, S. I. Csiszar, H. H. Hsieh, H.-J. Lin, C. T. Chen, and L. H. Tjeng, Phys. Rev. B **67**, 092404 (2003).
[59] T. Burnus, Z. Hu, M. W. Haverkort, J. C. Cezar, D. Flahaut, V. Hardy, A. Maignan, N. B. Brookes, A. Tanaka, H. H. Hsieh *et al.*, Phys. Rev. B **74**, 245111 (2006).
[60] T. Burnus, Z. Hu, H. H. Hsieh, V. L. J. Joly, P. A. Joy, M. W. Haverkort, H. Wu, A. Tanaka, H.-J. Lin, C. T. Chen *et al.*, Phys. Rev. B **77**, 125124 (2008).
[61] K. Baroudi, C. Yim, H. Wu, Q. Huang, J. H. Roudebush, E. Vavilova, H.-J. Grafe, V. Kataev, B. Buechner, H. Ji *et al.*, J. Solid State Chem. **210**, 195 (2014).
[62] M. A. Laguna-Marco, P. Kayser, J. A. Alonso, M. J. Martínez-Lope, M. van Veenendaal, Y. Choi, and D. Haskel, Phys. Rev. B **91**, 214433 (2015).
[63] S. Agrestini, K. Chen, C.-Y. Kuo, L. Zhao, H.-J. Lin, C.-T. Chen, A. Rogalev, P. Ohresser, T.-S. Chan, S.-C. Weng *et al.*, Phys. Rev. B **100**, 014443 (2019).
[64] H. Ebert, J. Phys.: Condens. Matter **1**, 9111 (1989).